






RESEARCH ARTICLE | MAY 07 2024

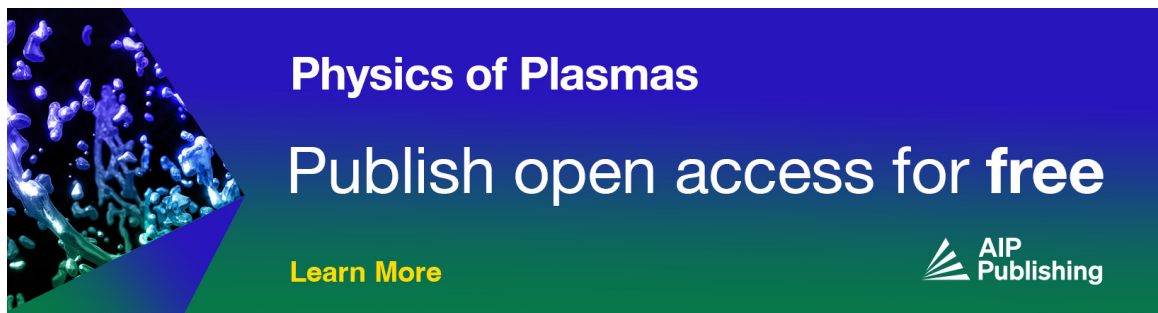
Fluid simulations of resistive drift-wave turbulence with diamagnetic flow in ZPED experiments

H. J. Zhao ; Y. Mao ; Z. Y. Wang; W. W. Xiao  ; Y. Xiao  




Phys. Plasmas 31, 052108 (2024)

<https://doi.org/10.1063/5.0190110>



Physics of Plasmas
Publish open access for free
[Learn More](#)



Fluid simulations of resistive drift-wave turbulence with diamagnetic flow in ZPED experiments

Cite as: Phys. Plasmas **31**, 052108 (2024); doi: [10.1063/5.0190110](https://doi.org/10.1063/5.0190110)

Submitted: 3 December 2023 · Accepted: 23 April 2024 ·

Published Online: 7 May 2024



View Online



Export Citation



CrossMark

H. J. Zhao,  Y. Mao,  Z. Y. Wang, W. W. Xiao, ^{a)}  and Y. Xiao ^{a)} 

AFFILIATIONS

Institute for Fusion Theory and Simulation, School of Physics, Zhejiang University, Hangzhou 310027, China

^{a)} Authors to whom correspondence should be addressed: wwwxiao@zju.edu.cn and yxiao@zju.edu.cn

ABSTRACT

We derive a diamagnetic resistive fluid model (DRF) and develop an associated two-dimensional fluid simulation code (DRF-2D) to explore the dynamics of resistive drift modes within the plasmas of the Zheda Plasma Experiment Device (ZPED). The validation of the linear dispersion relation for the DRF-2D code revealed a harmonious agreement between analytical theory and linear numerical simulations. Leveraging plasma parameters obtained from the ZPED experiments, we conducted a comprehensive series of nonlinear simulations using the DRF-2D code. Our simulations successfully replicate the nonlinear trends in turbulent fluctuations and transport observed in the ZPED experiments, particularly demonstrating a remarkably accurate alignment of the turning point in the magnetic field. Notably, the DRF model sheds light on the observed frequency sign reversal from the electron diamagnetic direction to the ion diamagnetic direction in the ZPED experiments. This is demonstrated through well-matched turning points in the confining magnetic field between the nonlinear simulations and ZPED experiments. The fidelity of our model in capturing these phenomena underscores its efficacy in providing valuable insights and predictive capabilities for the intricate dynamics observed in the ZPED plasmas.

© 2024 Author(s). All article content, except where otherwise noted, is licensed under a Creative Commons Attribution (CC BY) license (<https://creativecommons.org/licenses/by/4.0/>). <https://doi.org/10.1063/5.0190110>

I. INTRODUCTION

In the realm of magnetic fusion plasmas, understanding the intricate dynamics of turbulence transport is crucial for determining the efficacy of plasma confinement. Drift wave turbulence, a dominant source of low-frequency electromagnetic fluctuations in most fusion parameters, plays a pivotal role. Of particular interest is resistive drift wave (RDW) turbulence, prevalent at the periphery of fusion plasmas¹ and in linear devices.^{2–4} The Zheda Plasma Experiment Device (ZPED)⁵ has brought forth a noteworthy development, unveiling a nonlinear phenomenon with profound implications for plasma confinement. As the confining magnetic field strengthens, nonlinear turbulence fluctuations initially rise before reaching a saturation level. Concurrently, density gradients exhibit similar features, accompanied by a significant shift in wave direction near the critical field.⁶ The intriguing nonlinear relationship between magnetic field strength and confinement performance has garnered considerable attention.

The simplicity of the Hasegawa–Wakatani (HW) equations^{7,8} makes them a foundational plasma fluid model for exploring resistive drift turbulence and nonlinearity⁹ through extensive numerical simulations on cylindrical plasmas.^{10–13} In the context of ZPED experiments characterized by a uniform magnetic field and high resistivity, the

suitability of HW equations becomes evident. However, the observation of ion diamagnetic direction waves in the ZPED experiments under low magnetic fields,⁶ indicative of equilibrium ion diamagnetic flow, suggests the oversight of traditional theories and simulations in accounting for diamagnetic flow. Therefore, formulating and incorporating a model that considers diamagnetic flow in simulations becomes imperative for a comprehensive understanding. It is widely recognized that gyroviscosity cancellation can largely mitigate the diamagnetic flow contribution in the fluid momentum equation.^{14–16} Nonetheless, high-order effects may persist, and the ion diamagnetic flow effect may become pronounced when the finite Larmor radius (FLR) effect is substantial.

This paper is structured as follows: In Sec. II, we present the diamagnetic resistive fluid model (DRF) and introduce the development of a two-dimensional fluid code (DRF-2D) based on this model. Within the same section, we conduct an in-depth analysis of experimental parameters, considering the implications of ionization rates. The verification of DRF-2D is undertaken through an examination of linear resistive drift instability, detailed in Sec. III A. Moving on to Sec. III B, we delve into the nonlinear physics based on ZPED plasma parameters and experiments, utilizing nonlinear DRF-2D simulations. This exploration includes the observation of spectrum cascading and

the evolution of mode structure. Through a series of magnetic field scans detailed in Sec. III B, we uncover nonlinear turbulent transport and frequency sign reversal that align with observations from ZPED experiments. To encapsulate our findings, a summary of the main results is provided in Sec. IV.

II. SIMULATION MODEL

A. Diamagnetic resistive fluid model

Conventional HW model often overlook a diamagnetic flow effect, which becomes problematic when dealing with thermal ions possessing finite diamagnetic velocity $v_{D,i}$. In the ZPED device, a uniform magnetic field is reasonably assumed with $\mathbf{B} = B_0 \hat{z}$. Meanwhile, we assume roughly constant temperature in the device, i.e., $T_e = T_i = \text{constant}$, which is justified by the relatively small value of L_{Te}^{-1} and effective heat exchange observed between ions and electrons in experiments.⁶ Ions primarily experience perpendicular viscosity, whereas electrons are subject to parallel resistivity. Given the absence of end plates in the ZPED device, we assume an insulating boundary condition. It has been demonstrated that under this condition, the dominant instability is likely to be drift waves, whereas conducting boundary devices are more prone to sheath modes and Kelvin–Helmholtz instability.¹⁷ We further assume the parallel wavelength to be approximately equal to the length of the device, i.e., $\lambda_{\parallel} = L = 2 \text{ m}$. To further simplify the theoretical model, we introduce the subsidiary small FLR ordering parameter, $\Delta \sim k_{\perp} \rho \sim k_{\parallel} / k_{\perp} < 1$, and $\delta \sim \Delta^2$.

We first start from the ion momentum equation by ignoring the ion parallel motion:

$$m_i n_i (\partial_t + \mathbf{u}_i \cdot \nabla) \mathbf{u}_i + \nabla \cdot \boldsymbol{\pi}_f = q n_i (\mathbf{E} + \mathbf{u}_i \times \mathbf{B}) + \mu \nabla_{\perp}^2 \mathbf{u}_i - \nabla p_i, \quad (1)$$

where the term $\mu \nabla_{\perp}^2 \mathbf{u}_i$ is ion collisional viscosity, and $\boldsymbol{\pi}_f$ is the gyroviscosity. We use the gyroviscosity derived in previous theoretical work.¹⁶

$$\nabla \cdot \boldsymbol{\pi}_f = -n_0 m_i \mathbf{V}_* \cdot \nabla \mathbf{u}_1 + \nabla \tilde{\chi}_1 + \frac{p_{i0}}{2\Omega} \mathbf{b} \times \nabla (\nabla \cdot \mathbf{u}_2) - \frac{p_{i0}}{\Omega^2} \nabla^2 \frac{d\mathbf{u}_1}{dt}, \quad (2)$$

where $\mathbf{V}_* = \frac{\mathbf{b} \times \nabla p_0}{q n_0 B} + \frac{\mathbf{b} \times \nabla_{\perp} (\tilde{p}_1 + \tilde{\chi}_1)}{q n_0 B}$, $\tilde{\chi}_1 = -\frac{p_0}{2\Omega} \mathbf{b} \times (\nabla_{\perp} \times \tilde{\mathbf{u}}_{\perp 1})$, and $\mathbf{u}_1, \mathbf{u}_2$ are the first and second order perturbed flow, respectively. The gyroviscosity cancellation is included in the preceding expression. By balancing the first order terms in the preceding momentum equation, we can find

$$\mathbf{u}_1 = \frac{\mathbf{b} \times \nabla \tilde{\phi}_1}{B} + \frac{\mathbf{b} \times \nabla \tilde{p}_1}{q n_0 B} + \frac{\mathbf{b} \times \nabla \cdot \boldsymbol{\pi}_{f1}}{q n_0 B}. \quad (3)$$

To the lowest order¹⁶ in the δ expansion, $\nabla \cdot \boldsymbol{\pi}_{f1} = \nabla \tilde{\chi}_1$, and then we can obtain

$$\left(\frac{\tilde{\chi}_1}{p_{i0}} \right) \cong -\frac{Z \rho_s^2}{2} \nabla^2 \left(\tilde{\phi} + \frac{\tilde{n}}{Z\tau} \right). \quad (4)$$

By keeping terms to order δ^3 , the momentum equation can be written as

$$\frac{1}{\Omega} (1 - \rho_i^2 \nabla_{\perp}^2) (\partial_t + \mathbf{V}_E \cdot \nabla) \mathbf{u}_1 + \frac{\rho_i^2}{2} \mathbf{b} \times \nabla (\nabla \cdot \mathbf{u}_2) - \frac{\rho_i^2}{\Omega} \nabla^2 [\mathbf{V}_* \cdot \nabla \mathbf{u}_1] = \mathbf{u}_2 \times \mathbf{b}, \quad (5)$$

with which we can find the analytic expression for \mathbf{u}_2 . In addition, combining the ion continuity equation with the electron continuity equation gives

$$\nabla \cdot \mathbf{u}_2 = \frac{T_e}{m_e \nu_{ei}} \nabla_{\parallel}^2 (\phi_p - n_p), \quad (6)$$

where $\phi_p = \phi - \langle \phi \rangle$ and $n_p = n - \langle n \rangle$, $\langle \dots \rangle$ represents the poloidal average. We also note that the zonal component of the potential $\langle \phi \rangle$ does not contribute to the parallel current.

Inserting the expressions for \mathbf{u}_1 and \mathbf{u}_2 in the ion momentum equation, we can obtain the following normalized vorticity equation:

$$\begin{aligned} \partial_t \left[\left(1 - \frac{3}{2\tau} \nabla_{\perp}^2 \right) \nabla_{\perp}^2 \tilde{\phi} \right] \\ = - \left[\left(1 - \frac{3}{2\tau} \nabla_{\perp}^2 \right) \nabla_{\perp}^2 \frac{\partial_t \tilde{n}}{Z\tau} \right] - \nabla_{\perp} \cdot \left[(\mathbf{V}_E \cdot \nabla_{\perp}) \nabla_{\perp} \left(\tilde{\phi} + \frac{\tilde{n}}{Z\tau} \right) \right] \\ - \frac{C_r}{Z} \left(1 + \frac{1}{2\tau} \nabla_{\perp}^2 \right) \nabla_{\parallel}^2 (\tilde{\phi}_p - \tilde{n}_p) + \frac{1}{\tau} \nabla_{\perp}^2 \nabla_{\perp} \cdot \left[\mathbf{V}_* \cdot \nabla_{\perp} \nabla_{\perp} \left(\tilde{\phi} + \frac{\tilde{n}}{Z\tau} \right) \right] + C_{\mu} \nabla_{\perp}^4 \left(\tilde{\phi} + \frac{\tilde{n}}{Z\tau} \right), \end{aligned} \quad (7)$$

where the ion charge Z may not be unity, and the normalization is given by $t_u = 1/\Omega_{ci}$, $x_u = \rho_s$, $\tilde{n} = n_1/n_0$, and $\tilde{\phi} = e\phi/T_e$. The other constants in the preceding equations are given by $C_r = \frac{m_i \Omega_{ci}}{m_e \nu_{ei}}$, $C_{\mu} = \frac{\mu \Omega_{ci}}{n_i T_e}$. If we use $\mu = \frac{3}{10} \frac{n_i T_i \nu_{ii}}{\Omega_{ci}^2}$,¹⁸ then $C_{\mu} = \frac{3}{10} \frac{T_i \nu_{ii}}{T_e \Omega_{ci}}$. The normalized electron continuity equation becomes

$$\left(\frac{\partial}{\partial t} + \mathbf{V}_E \cdot \nabla_{\perp} \right) \tilde{n} + \mathbf{V}_E \cdot \nabla \ln n_0 + C_r \nabla_{\parallel}^2 \left(\tilde{\phi}_p - \tilde{n}_p \right) = 0. \quad (8)$$

The DRF equations (7) and (8) are nonlinear and cannot be solved analytically in general. In order to solve Eqs. (7) and (8) numerically, we have developed a two-dimensional fluid code DRF-2D to solve the preceding DRF equations. In this code, we treat the parallel wave spectrum in the z -direction as a single parallel mode and employ spectral method¹⁹ in cylindrical coordinates (r, θ) to solve for the perpendicular motion. To advance in time, our code employs a second-order Runge–Kutta scheme for a balance of accuracy and efficiency. When pushing Eq. (2), $(\nabla_{\perp}^2 - 3/2\tau \nabla_{\perp}^4) \tilde{\phi}$ directly, then we perform $(\nabla_{\perp}^2 - 3/2\tau \nabla_{\perp}^4)^{-1}$ to obtain the electric potential. This can be done by solving the inverse matrix of the spectral differential matrix.

III. SIMULATION RESULTS

A. Simulation settings based on the ZPED experiment

Recent ZPED experiments have observed many interesting turbulence phenomena (ZPED) via altering the confining magnetic field,^{5,6} which requires numerical simulation to interpret the underlying physics. The ZPED device maintains a cylindrical plasma with length $L_0 = 2 \text{ m}$, and radius $a_0 = 0.15 \text{ m}$, and is capable of generating a uniform magnetic field of up to 0.2 T .

Our investigation begins with a magnetic field strength of $B = 1000 \text{ G}$, near the nonlinear turning point. We set the other ZPED plasma parameters as follows: $n_e(r=0) = 4.5 \times 10^{17} \text{ m}^{-3}$, $T_e = 2.3 \text{ eV}$. For this plasma, the electron–ion collision rate $\nu_{ei} = 4.05 \times 10^6 \text{ rad/s}$ is sufficiently high to maintain thermal equilibrium between ions and

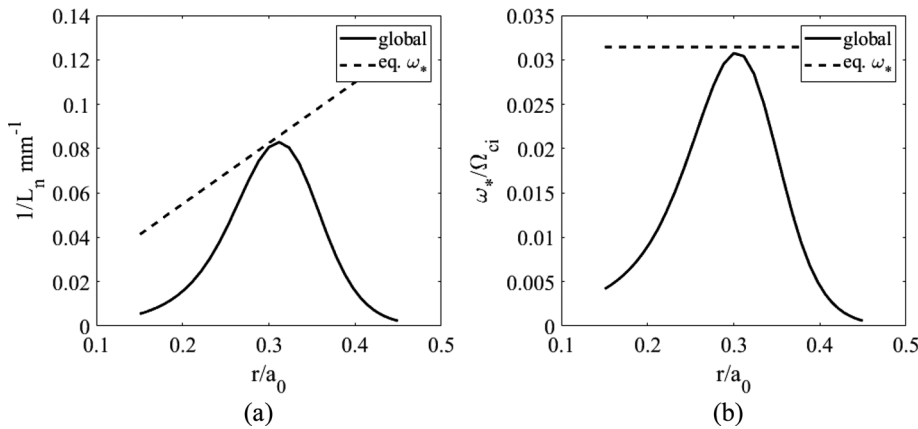


FIG. 1. Plasma profiles employed in the simulations vary with $1/L_n$ for equal ω_* values. (a) Profiles depicting L_n^{-1} and (b) corresponding ω_* ($m = 1$) profiles along the radial direction.

electrons, allowing us to assume $T_i = T_e$. The inverse density gradient scale length, L_n^{-1} , reaches its maximum value of 0.0825 mm^{-1} at $r = 0.3a_0$. In addition, we have constructed the density profile using the following analytic formula, as shown in Fig. 1:

$$n_e = n_{e0} \left[1 + c_1 \left(\frac{c_2 - \frac{r^2}{a^2}}{c_3} - 1 \right) \right], \quad (9)$$

with $[c_1, c_2, c_3] = [0.41, 0.075, 0.04]$. Figures 1(a) and 1(b) also demonstrate the equal- L_n^{-1} or equal- ω_* profiles, whose form were given by $L_n^{-1}(r) = \exp(-0.5r^2 L_n^{-1}(0.3a_0)/0.3a_0)$. The latter profile is flat and represents the local profile model, which is usually employed to verify the linear dispersion relation.

The ZPED employs nitrogen as the working gas, which raises the question of determining the appropriate ion charge number (Z) for the ZPED plasmas. Assuming local thermal equilibrium, the density components adhere to the following double temperature Saha equation:²⁰

$$n_e \frac{n_i^{b+1}}{n_a} = 2 \frac{z_1(T_e)}{z_0(T_e)} \frac{(2\pi m_e k_B T_e)^{\frac{3}{2}}}{h^3} \exp\left(-\frac{E_{i,1} - \Delta E_{i,1}}{k_B T_e}\right), \quad (10)$$

$$n_e \frac{n_i^{b+1}}{n_i^b} = 2 \frac{z_{b+1}(T_e)}{z_b(T_e)} \frac{(2\pi m_e k_B T_e)^{\frac{3}{2}}}{h^3} \exp\left(-\frac{E_{i,b+1} - \Delta E_{i,b+1}}{k_B T_e}\right), \quad (11)$$

where n_a represents the neutral particle density, n_b represents the particle density for N^{b+} ion, $E_{i,b}$ denotes the ionization energy, and $\Delta E_{i,b}$ represents the correction energy due to Debye shielding, although we disregard this correction in our calculations. $2z_{b+1}/z_b$ signifies the ratio of partition functions, which is close to unity. The outcomes of our calculations for the first six components are depicted in Fig. 2. The figure illustrates that the ionization rate is nearly 100% and N^{3+} ions dominate the primary region of interest. However, it is important to note that the Saha equation holds for the ionization process under local thermal equilibrium. Given that the helicon source operates under power constraints and the system may not stay in complete thermal equilibrium, the ionization rate is influenced not only by local temperature but also by complex global conditions. In our nonlinear simulations, we find that setting $Z = 1$ is more appropriate for reproducing experimental observations. Thus, we make a convenient assumption that the ionization rate is nearly 100%, and N^+ is the predominant species. In the subsequent phase of our simulation, we will primarily focus on the $Z = 1$ case, although we will also examine the $Z = 3$ case

for comparison. The precise determination of charge number and ionization rates is reserved for future experimental investigations.

For simplicity, we assume zero boundary conditions in the simulation at $r = 0.15a_0$ and $r = 0.45a_0$. This choice is made by considering the limitations of the helicon source power, which is unable to fully ionize the gas at the core. Furthermore, the density gradient is most pronounced at $r = 0.3a_0$, making it a suitable boundary for our radial simulation region. This approach also helps avoid potential singularity issues when approaching $r = 0$. After a convergence study, the number of radial grids is set as $N_r = 40$, the number of azimuthal grids is set as $N_\theta = 160$ points, and the time step to advance simulation is set to $dt = 0.1\Omega_{ci}^{-1}$.

B. Linear simulation results

To examine the linear physics, we work within a slab geometry and assume Fourier form in the azimuthal or y -direction, i.e., electrostatic potential fluctuation $\tilde{\phi}(x, y, t) = \phi(x)e^{i(ky - \omega t)}$, and density fluctuation $\tilde{n}(x, y, t) = n(x)e^{i(ky - \omega t)}$. We take $k = m/0.3a_0$, where m is the poloidal mode number, a_0 is the plasma column radius, and $0.3a_0$

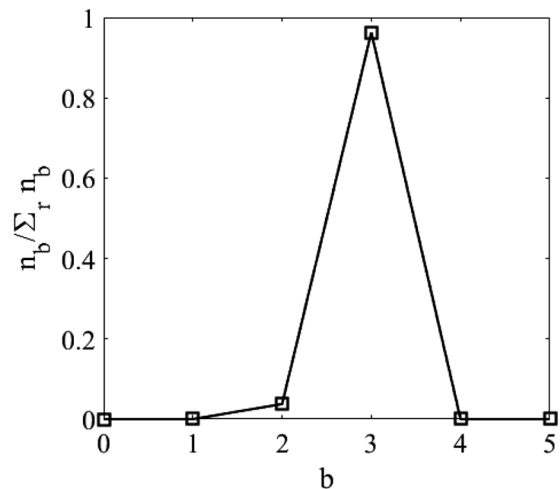


FIG. 2. The density component distribution in nitrogen plasma, obtained by solving Eqs. (8) and (9) up to $r = 5$, reveals the dominance of N^{3+} ions in the nitrogen ion population.

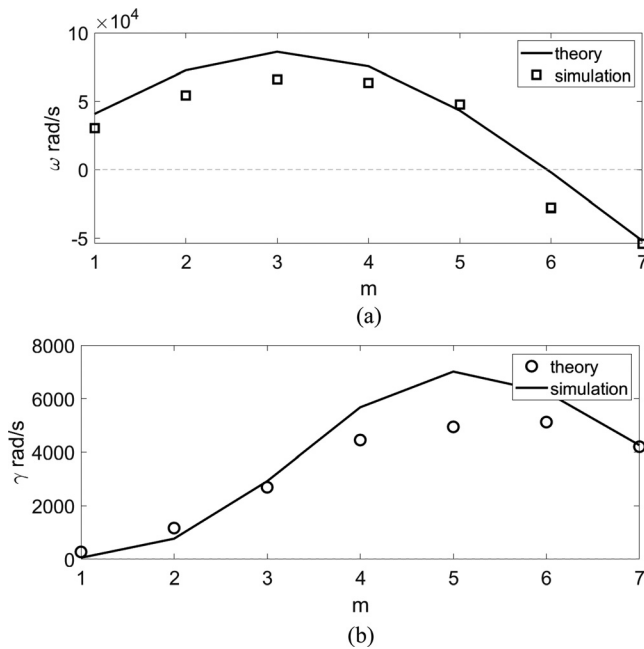


FIG. 3. Linear frequency (a) and growth rate (b) vs poloidal mode number m for $Z = 1$ and $B = 1000$ Gs.

is the peak position of the density gradient profile. Subsequently, we derive the linear dispersion relation for the DRF model by linearizing Eqs. (7) and (8) while retaining solely the first-order terms:

$$-i\omega\tilde{n}_k + i\omega_{*e}\tilde{\phi}_k - C_r k_{\parallel}^2 (\tilde{\phi}_k - \tilde{n}_k) = 0, \quad (12)$$

$$k^2 \left(1 + \frac{3}{2Z^2\tau} k^2\right) (-i\omega) \left(\tilde{\phi}_k + \frac{\tilde{n}_k}{Z\tau}\right) + \left(1 - \frac{k^2}{2Z^2\tau}\right) k_{\parallel}^2 (\tilde{\phi}_k - \tilde{n}_k) + \frac{ik^4\omega_{*i}}{Z^2\tau} \left(\tilde{\phi}_k + \frac{\tilde{n}_k}{Z\tau}\right) + C_{\mu} k^4 \left(\tilde{\phi}_k + \frac{\tilde{n}_k}{Z\tau}\right) = 0. \quad (13)$$

Numerically solving Eqs. (12) and (13) yields the dispersion relation. As $T_i \rightarrow 0$, we can retrieve the dispersion relation for resistive drift wave (RDW) under the assumption of cold ions.²¹ It is known that RDW mainly propagates in the electron diamagnetic direction. From the numerical dispersion relation plotted against the poloidal mode number m , as shown by the solid lines in Fig. 3, it becomes evident that the negative real frequency ω_r is achievable when the wavelength is sufficiently small, which suggests that RDW can propagate in the ion diamagnetic direction in the low magnetic field limit. This observation opens up possibilities for elucidating the frequency shift observed in the ZEPD experiments.

In order to validate the linear physics of the DRF-2D code, we utilize the profiles displayed in Fig. 1, which ensures that ω_* is uniform in the radial direction. The linear simulation results are presented in Fig. 3 for the case with $Z = 1$ and $B = 1000$ Gs. Upon comparing with

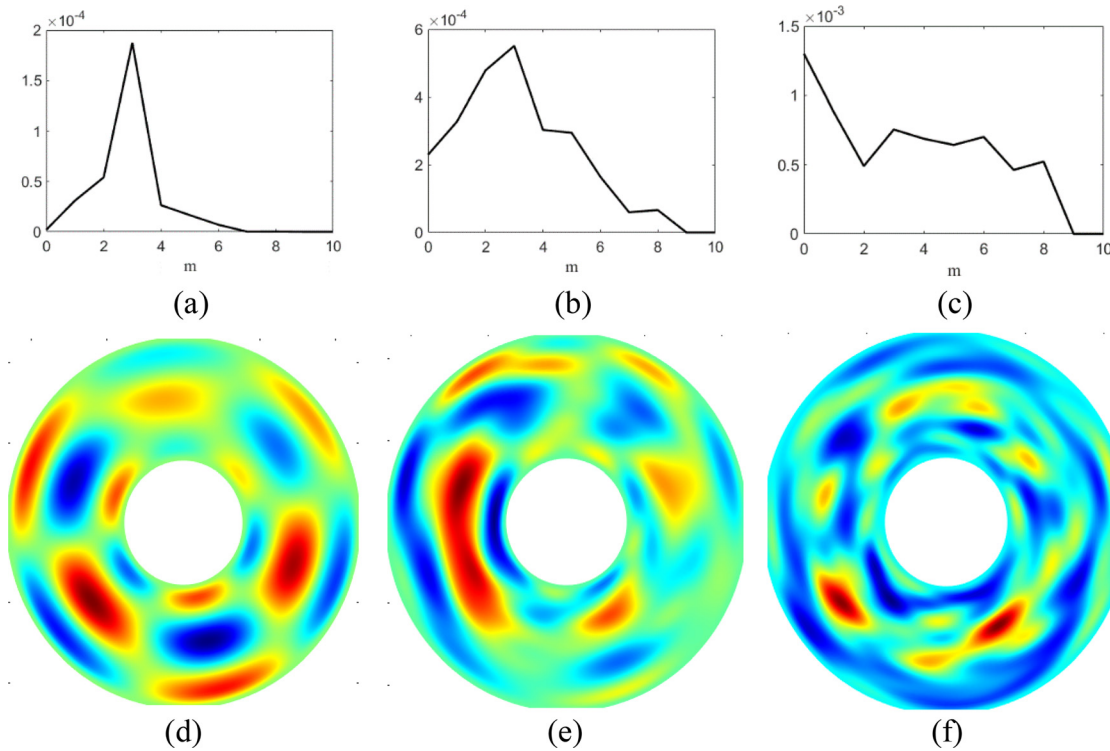


FIG. 4. Density mode structures obtained from nonlinear simulations with $Z = 1$, $B = 1000$ Gs. The m -spectra at $t = 1500, 2700, 5100(\Omega_{Ci}^{-1})$ are presented in (a)–(c), respectively. Corresponding 2D mode structures are depicted in (d)–(f).

the theoretical predictions in Eq. (6), it becomes evident that, for the local profile, the real frequencies and growth rates closely align with the analytical theory, albeit with some noticeable differences.

C. Nonlinear simulation for the ZPED plasmas

All azimuthal modes were retained in the DRF-2D simulations, allowing them to progress nonlinearly until reaching saturation. This approach was adopted to capture turbulent transport phenomena for direct comparison with observations from the ZPED experiments. It is

noteworthy that the original Hasegawa–Wakatani equations are well-regarded for their capability to address nonlinear mode-mode coupling processes.²² The utilization of multiple-mode nonlinear simulations is anticipated to align the nonlinear plasma behaviors of the DRF system with experimental diagnostics.^{5,6}

1. Evolution of azimuthal wave spectrum

The ZPED experiments reveal a concentration of turbulence spectra in the low- m range, characterized by azimuthal wave numbers m

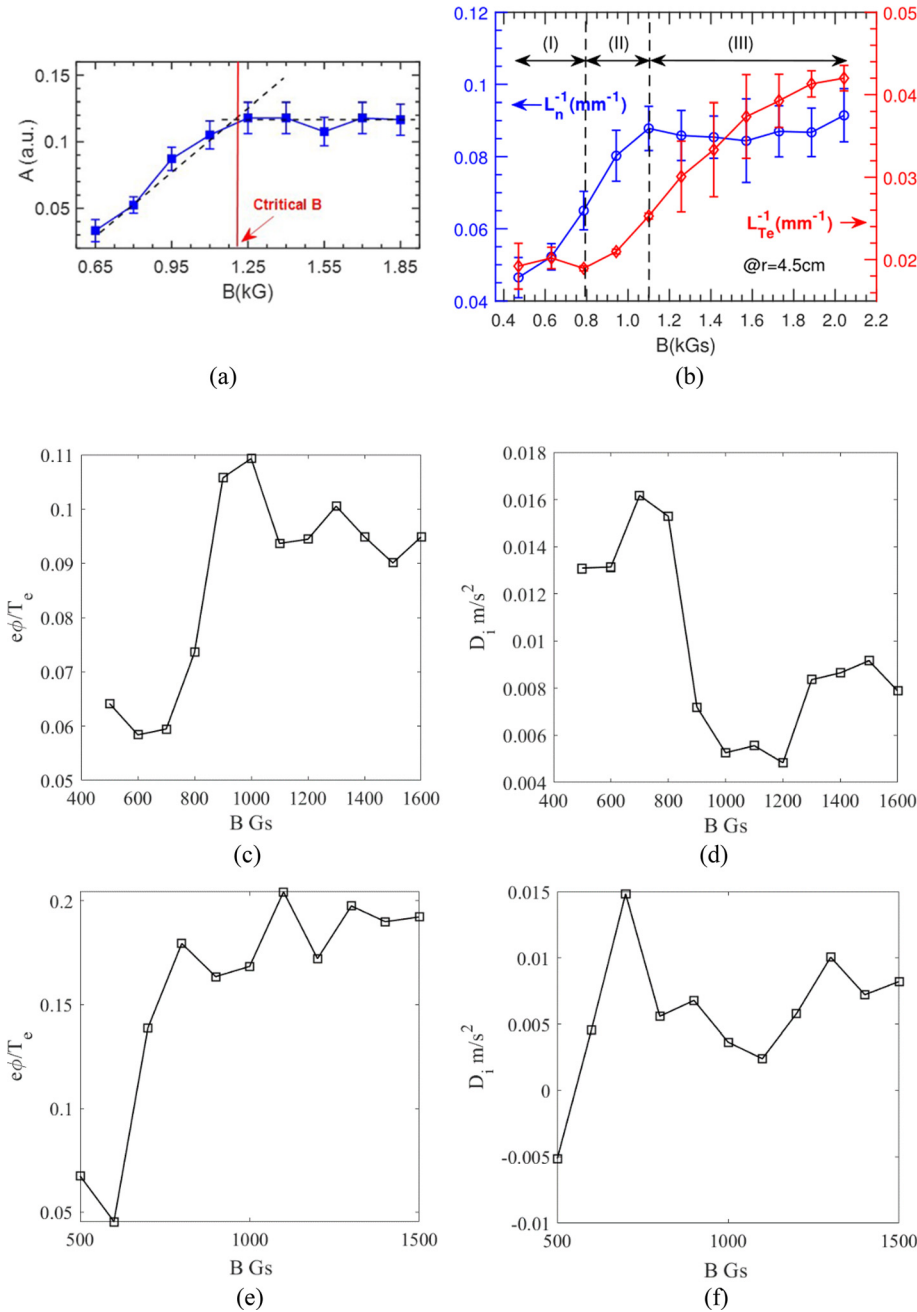


FIG. 5. Panels (a) and (b): Experimental results^{5,6} of turbulence perturbation and profiles with increasing magnetic field. Nonlinear simulation results employing the DRF-2D code depicting the evolution with increasing magnetic field (B) for $Z = 1$ [panels (c) and (d)] and $Z = 3$ [panels (e) and (f)]. Panels (c) and (d) showcase the normalized nonlinearly saturated electric potential, while Panels (e) and (f) display particle diffusivity.

20 May 2024 08:54:45

ranging from 1 to 5. The linear dispersion relation predicts the fastest growing mode to be the $m = 5$ mode for linear modes. However, during the nonlinear saturation of DRF-2D simulations, we observe a cascade in the azimuthal mode spectrum toward smaller m directions, accompanied by the excitation of zonal flows. This reproduction results in an azimuthal mode spectrum akin to that observed in experiments.

As illustrated in Figs. 4(a) and 4(d), when $Z = 1$, $B = 1000$ Gs, and $\Omega_{ci}t = 1500$, the dominant mode during the linear stage is $m = 3$. By $\Omega_{ci}t = 2700$, the system enters the saturation phase, with the spectrum beginning to broaden. In the fully saturated nonlinear stage ($\Omega_{ci}t = 5100$), the perpendicular structure continues to evolve to longer and shorter wavelengths, with the $m = 3-6$ mode becoming dominant in the azimuthal mode spectrum, consistent with experimental observations.⁶ Figures 4(b) and 4(c) reveal a significant $m = 0$ zonal flow component in the azimuthal mode spectrum during nonlinear turbulence. In summary, it is crucial to understand the experimental

observation of low- m modes by considering the significant broadening in the azimuthal mode spectrum and the generation of zonal flow during the nonlinear saturation of resistive drift mode.

2. Fluctuations and transport vs magnetic field

As the confining magnetic field B varies, our nonlinear DRF-2D simulations exhibit similar characteristics to those observed in experiments, as shown in Fig. 5. Initially, electric potential fluctuations increase as B increases. However, a turning point occurs at approximately $B = 900$ Gs, beyond which the fluctuations begin to saturate as B continues to increase.⁵ A corresponding regularity is observed in the density gradient scale length L_n^{-1} .⁶ To comprehensively assess the effect of magnetic field B , we conduct a parameter scan via varying B and measuring the corresponding saturation levels of nonlinear potential fluctuations $\tilde{\phi}$ and particle diffusivity D_i . We computed the $\tilde{\phi}$

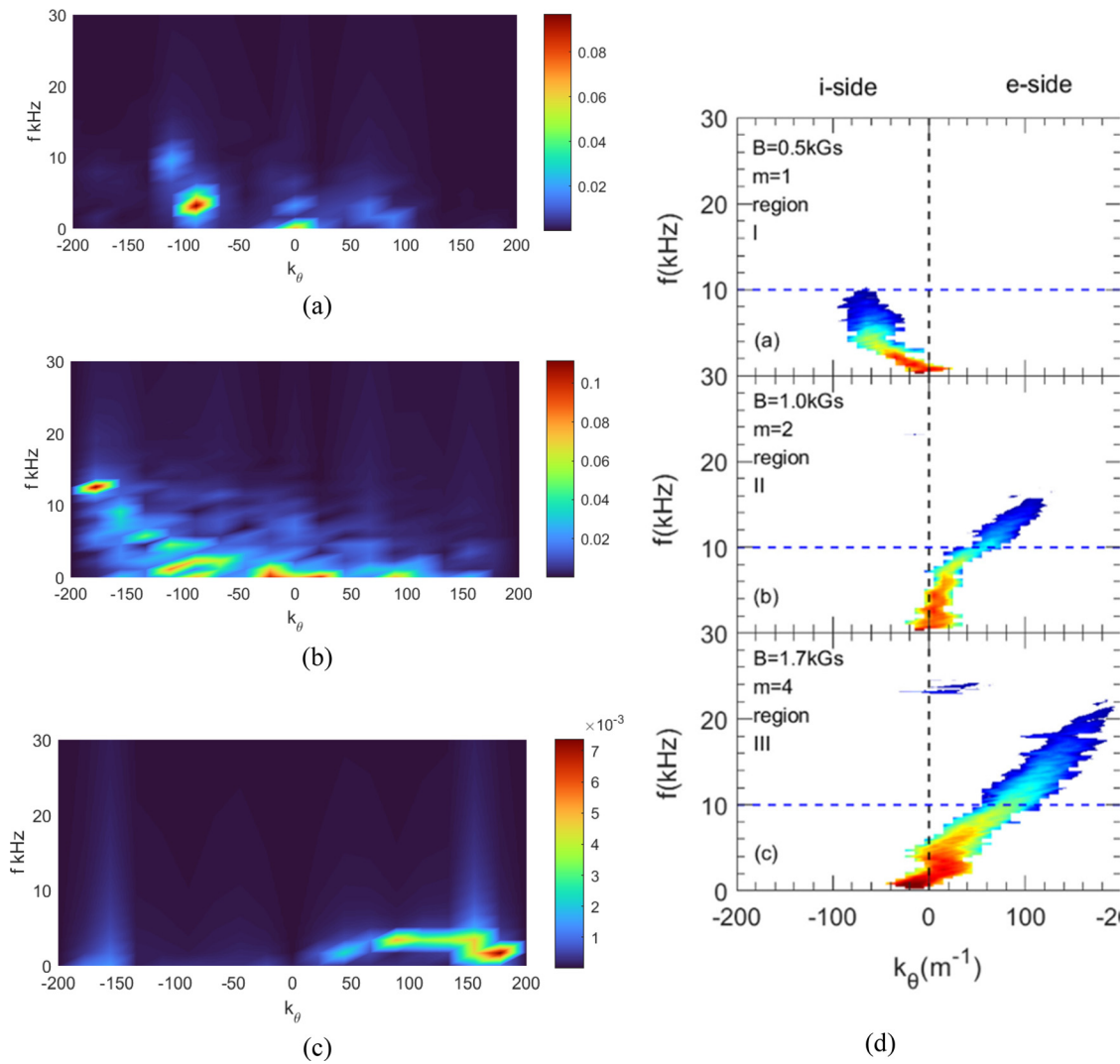


FIG. 6. The ω - m spectrum of electric potential under different confining magnetic fields: (a) $B = 700$ Gs, (b) $B = 1000$ Gs, and (c) $B = 1500$ Gs. (d) $k_\theta - f$ spectrum for turbulence in the ZPED experiment.⁵

levels by calculating the root mean square value on the reference flux surface at $r = 0.3a_0$, and the particle diffusivity D_i was determined through azimuthal averaging at $r = 0.3a_0$, given by $D_i = L_n \langle \tilde{n} v_{E,r} \rangle_{r=0.3a_0} / n_0$.

In the course of conducting B scanning simulations with $Z = 1$, we pinpointed the critical magnetic field for both $\tilde{\phi}$ and D_i at 900 Gs. The level of potential fluctuations, serving as a turbulence strength indicator, exhibits a trend closely resembling experimental observations during B field scans. The nonlinear behavior of the particle transport coefficient elucidates the observed trend in L_n^{-1} in the ZPED experiments.⁶ Specifically, as the magnetic field gradually increases but stays below 900 Gs, D_i decreases, suggesting an enhancement in confinement and hinting at a potential formation of a steeper density gradient and transport barrier. Conversely, when the magnetic field surpasses the critical value ($B = 900$ Gs), the predicted D_i remains relatively constant, signifying a stable confinement scenario with minimal variation in L_n^{-1} .

For the $Z = 3$ case, illustrated in Fig. 5, both the critical magnetic fields for $\tilde{\phi}$ and D_i are identified at 800 Gs. The trend of $\tilde{\phi}$ mirrors that of experiments and the $Z = 1$ case, where normalized electric potentials initially increase and then maintain a constant level. As the magnetic field B increases, D_i exhibits an initial growth from nearly zero. Beyond a critical value, $B = 800$ Gs, the particle diffusivity D_i gradually decreases. Notably, the magnitudes of $\tilde{\phi}$ and D_i for the $Z = 3$ case are substantially smaller than those for the $Z = 1$ case, underscoring the sensitivity of fluctuation and transport to the ion charge number Z . It is evident that the trends in the electric fluctuation and particle diffusivity observed in the ZPED experiments align more closely with the $Z = 1$ case in the nonlinear DRF-2D simulations. Therefore, we can confidently assert that nonlinear simulations employing the DRF-2D code effectively explain the critical nonlinear characteristics observed in the ZPED experiments when assuming the N^+ ions as the dominant ion component.

An intriguing phenomenon unique to the DRF model is the reversal in frequency sign, transitioning from the ion diamagnetic direction to the electron diamagnetic direction with an increasing magnetic field strength, as illustrated in Fig. 6. This observation concurs with experimental findings, where a change in wave propagation direction is noted at approximately $B = 1000$ Gs.⁶ In our simulations, the predominant mode exhibits ion diamagnetic characteristics during the linear stage when the magnetic field is below 900 Gs, with no significant evidence of inverse cascading in the azimuthal spectrum. However, beyond the critical value, the azimuthal spectrum initiates a cascade toward a low m -mode dominated spectrum, propagating in the electron diamagnetic direction.

It is noteworthy that, in the context of the conventional Hasegawa–Wakatani equations, a change in wave propagation direction is deemed impossible due to the absence of ion diamagnetic flow. Contrary to the $Z = 3$ DRF model, in which no frequency sign change occurs after nonlinear saturation, our observations provide robust evidence favoring the $Z = 1$ DRF model. This underscores the distinctive capability of the $Z = 1$ model in capturing and explaining the observed frequency sign reversal, further strengthening the case for its superiority over the $Z = 3$ DRF model.

The remarkable alignment observed between the experimental results and the ($Z = 1$) DRF-2D nonlinear simulations strongly supports the presence of ion diamagnetic flow within the ZPED linear device. The observed frequency sign reversal and variations in

turbulence transport under different magnetic field conditions suggest a potential link to the nonlinear cascading of the turbulence spectrum. Initially, the instability grows faster, particularly with higher m modes. In scenarios with sufficiently confining magnetic fields, the turbulence undergoes cascading into low m turbulence, predominantly propagating in the electron diamagnetic direction. Conversely, under conditions of relatively low confining magnetic fields, the turbulence fails to cascade into a low- m spectrum, and the turbulence modes persist in the ion diamagnetic direction. In the regime dominated by ω_{*e} , the turbulence displays a notable combination of high fluctuation levels and low particle transport. This characteristic may hold significance for particle confinement within the ZPED, emphasizing the importance of understanding and manipulating turbulence dynamics in optimizing particle behavior within the system.

IV. CONCLUSIONS

Our work has yielded significant advancements in understanding the complex dynamics of resistive fluid systems, particularly in the context of the ZPED experiments. The formulation of the resistive fluid model DRF, which integrates diamagnetic flow effects into the traditional HW equation, has enabled us to develop the DRF-2D code. Through rigorous testing, we successfully validated the linear dispersion relation for resistive drift waves, aligning our numerical results from DRF-2D with analytical dispersion.

The nonlinear simulations conducted using DRF-2D unveiled intriguing phenomena, notably the observed inverse cascading in the azimuthal spectrum exclusive to the $Z = 1$ case. This phenomenon accurately reproduced a perpendicular mode structure akin to experimental findings in ZPED. Magnetic field scans in our simulations further demonstrated a compelling correlation between the saturated electric potential and the turbulent particle diffusivity, closely mirroring experimental data and providing insights into the observed change in L_n^{-1} in recent ZPED experiments.

A noteworthy discovery in our investigation was the frequency sign change near the critical magnetic field, highlighting the indispensable role of diamagnetic flow in linear devices. Considering the composition of ZPED plasmas according to the Saha equation, our nonlinear simulations challenge the conventional belief that N^{3+} is the dominant ion component. Instead, our findings favor the $Z = 1$ model over the $Z = 3$ model, suggesting that N^+ may be the prevalent ion species in the ZPED plasmas.

Looking ahead, our future research will focus on investigating the various factors that can contribute to the nonlinear critical magnetic field, including resistivity, viscosity, diamagnetic flow, and equilibrium flow. Additionally, incorporating temperature perturbations in the DRF model may be essential for understanding heat transport in the ZPED plasmas. A more comprehensive theoretical and simulation investigation is needed to elucidate the distinct transport characteristics on both sides of the turning point in the confining magnetic field.

ACKNOWLEDGMENTS

The authors thank the enlightening discussions with Professor Liu Chen, and we also thank H. W. Yang, C. Y. Wang, J. T. Ma, B. B. Jia, and G. X. Li for many valuable suggestions and conversations. This work is supported by the National MCF Energy R & D Program of China under Grant No. 2019YFE03060000 and by NSFC under Grant No. 12275013.

AUTHOR DECLARATIONS

Conflict of Interest

The authors have no conflicts to disclose.

Author Contributions

H. J. Zhao: Conceptualization (lead); Data curation (lead); Formal analysis (lead); Investigation (lead); Methodology (lead); Project administration (equal); Software (lead); Validation (lead); Visualization (lead); Writing – original draft (lead); Writing – review & editing (equal). **Y. Mao:** Data curation (supporting); Resources (supporting). **Z. Y. Wang:** Data curation (supporting); Resources (supporting). **W. W. Xiao:** Conceptualization (equal); Funding acquisition (equal); Investigation (equal); Methodology (equal); Project administration (lead); Resources (lead); Supervision (lead); Writing – review & editing (equal). **Y. Xiao:** Conceptualization (equal); Investigation (equal); Methodology (equal); Project administration (equal); Resources (equal); Supervision (equal); Writing – original draft (equal); Writing – review & editing (equal).

DATA AVAILABILITY

The data that support the findings of this study are available from the corresponding authors upon reasonable request.

REFERENCES

- ¹A. Hasegawa and M. Wakatani, “Plasma edge turbulence,” *Phys. Rev. Lett.* **50**(9), 682–686 (1983).
- ²P. Vaezi, C. Holland, S. C. Thakur, and G. R. Tynan, “Validation study of a drift-wave turbulence model for CSDX linear plasma device,” *Phys. Plasmas* **24**(9), 092310 (2017).
- ³P. Rosenau and D. Degani, “Thermal and radiation losses in a linear device,” *Phys. Fluids* **23**(11), 2318 (1980).
- ⁴B. Friedman, T. A. Carter, M. V. Umansky, D. Schaffner, and B. Dudson, “Energy dynamics in a simulation of LAPD turbulence,” *Phys. Plasmas* **19**(10), 102307 (2012).
- ⁵W. W. Xiao, C. Y. Wang, J. X. Zhu, N. Wali, K. Wang, Z. M. Sheng, and G. Y. Fu, “Observation of a nonlinear phenomenon of the density fluctuations on Zheda plasma experiment device (ZPED),” *AIP Adv.* **9**(7), 075026 (2019).
- ⁶C. Y. Wang, W. W. Xiao, Y. Ren, P. H. Diamond, X. B. Peng, J. T. Ma, and W. J. Zhong, “Intrinsic evolution of the decoupling and coupling of the plasma density and temperature in a cylindrical laboratory plasma device,” *Phys. Plasmas* **30**, 062303 (2023).
- ⁷M. Wakatani and A. Hasegawa, “A collisional drift wave description of plasma edge turbulence,” *Phys. Fluids* **27**(3), 611 (1984).
- ⁸A. Hasegawa and M. Wakatani, “Self-organization of electrostatic turbulence in a cylindrical plasma,” *Phys. Rev. Lett.* **59**(14), 1581–1584 (1987).
- ⁹J. W. Connor and O. P. Pogutse, “On the relationship between mixing length and strong turbulence estimates for transport due to drift turbulence,” *Plasma Phys. Controlled Fusion* **43**(2), 155–175 (2001).
- ¹⁰C. Holland, G. R. Tynan, J. H. Y. A. James, D. Nishijima, M. Shimada, and N. Taheri, “Numerical simulations of collisional drift-wave turbulence in a magnetized plasma column,” *Plasma Phys. Controlled Fusion* **49**(5A), A109–A119 (2007).
- ¹¹Ö. D. Gürçan, J. Anderson, S. Moradi, A. Biancalani, and P. Morel, “Phase and amplitude evolution in the network of triadic interactions of the Hasegawa–Wakatani system,” *Phys. Plasmas* **29**(5), 052306 (2022).
- ¹²N. Kasuya, M. Yagi, and K. Itoh, “Simulation of resistive drift wave turbulence in a linear device,” *J. Plasma Phys.* **72**(06), 957 (2006).
- ¹³N. Kasuya, M. Yagi, M. Azumi, K. Itoh, and S.-I. Itoh, “Numerical simulation of resistive drift wave turbulence in a linear device,” *J. Phys. Soc. Jpn.* **76**(4), 044501 (2007).
- ¹⁴F. L. Hinton and C. W. Horton, “Amplitude limitation of a collisional drift wave instability,” *Phys. Fluids* **14**(1), 116–123 (1971).
- ¹⁵C. T. Hsu, R. D. Hazeltine, and P. J. Morrison, “A generalized reduced fluid model with finite ion-gyroradius effects,” *Phys. Fluids* **29**(5), 1480–1487 (1986).
- ¹⁶Z. Chang and J. D. Callen, “Generalized gyroviscous force and its effect on the momentum balance equation,” *Phys. Fluids B: Plasma Phys.* **4**(7), 1766–1771 (1992).
- ¹⁷P. Vaezi, C. Holland, S. C. Thakur, and G. R. Tynan, “Understanding the impact of insulating and conducting endplate boundary conditions on turbulence in CSDX through nonlocal simulations,” *Phys. Plasmas* **24**(4), 042306 (2017).
- ¹⁸S. Tsai, “Thermal conductivity and low frequency waves in collisional plasmas,” *Phys. Fluids* **13**(8), 2108 (1970).
- ¹⁹T. L. Nicholas, *Spectral Methods in MATLAB* (Society for Industrial and Applied Mathematics, Philadelphia, PA, 2000).
- ²⁰X. Chen and P. Han, “On the thermodynamic derivation of the Saha equation modified to a two-temperature plasma,” *J. Phys. D: Appl. Phys.* **32**(14), 1711–1718 (1999).
- ²¹P. M. Bellan, *Fundamentals Plasma Physics* (Cambridge University Press, 2006).
- ²²P. H. Diamond, A. Hasegawa, and K. Mima, “Vorticity dynamics, drift wave turbulence, and zonal flows: A look back and a look ahead,” *Plasma Phys. Controlled Fusion* **53**(12), 124001 (2011).